

# An implementation of nuclear time-dependent density-functional theory and its application to the nuclear isovector electric dipole resonance

Yue Shi (石跃),<sup>1,\*</sup> Nobuo Hinohara,<sup>2,3</sup> and Bastian Schuetrumpf<sup>4</sup>

<sup>1</sup>*Department of Physics, Harbin Institute of Technology, Harbin 150001, People's Republic of China*

<sup>2</sup>*Center for Computational Sciences, University of Tsukuba, Tsukuba 305-8577, Japan*

<sup>3</sup>*Faculty of Pure and Applied Sciences, University of Tsukuba, Tsukuba 305-8571, Japan*

<sup>4</sup>*GSI Helmholtzzentrum für Schwerionenforschung, Planckstraße 1, 64291 Darmstadt, Germany*

**Background** Time-dependent density-functional theory (TDDFT) continues to be useful in describing a multitude of low-energy static and dynamic properties. In particular, with recent advances of computing capabilities, large-scale TDDFT simulations are possible for fission dynamics as well as isovector dipole (IVD) resonances.

**Purpose** Following a previous paper [Y. Shi, Phys. Rev. C 98, 014329(2018)], we present an extension of the density-functional theory to allow for dynamic calculations based on the obtained static Hartree-Fock results. We perform extensive benchmark calculations, by comparing the calculated results with that of an existing code Sky3D. To perform linear-response calculations using the TDDFT method, comparisons have been made with the finite-amplitude quasiparticle random-phase approximation (FAM-QRPA) method. We plan to apply the TDDFT method to a systematic description of the IVD resonances in the Zr, Mo, and Ru isotopes.

**Methods** The strengths of IVD resonances are calculated using two complementary methods: TDDFT and FAM-QRPA methods. For the TDDFT results, additional benchmark calculations have been performed using the well-tested code Sky3D. In these three models, the important ingredients which have major influence on the results, such as time-odd potentials, boundary conditions, smoothing procedures, spurious peaks etc., have been carefully examined.

**Results** The current TDDFT and the Sky3D codes yield almost identical response functions once both codes use the same time-odd mean fields and absorbing boundary conditions. The strengths of the IVD resonances calculated using the TDDFT and FAM-QRPA methods agree reasonably well with the same position of the giant dipole resonance. Upon seeing a reasonable accuracy offered by the implemented code, we perform systematic TDDFT calculations for spherical Zr and Mo isotopes near  $N = 50$ , where experimental data exist. For neutron-rich Zr, Mo, and Ru isotopes where shape evolution exist we predict the photoabsorption cross sections based on oblate and triaxial minima.

**Conclusions** The TDDFT code provides reasonable description for IVD resonances. Applying it to the spherical Zr and Mo nuclei, a reasonable agreement with experimental data has been achieved. For neutron-rich Zr isotopes, the photoabsorption cross section based on the two coexisting minima reflects the feature of the deformation of the minima.

PACS numbers:

## I. INTRODUCTION

Since its first numerical realizations in the late 70s [1–3], the time-dependent density-functional theory (TDDFT) continues to be useful in describing a variety of low-energy nuclear static and dynamic properties, ranging from the linear response of nuclear density, to the large-amplitude motion of heavy nuclei [4–8].

The modern developments [9–11] allow for the inclusion of the full original Skyrme density-functional theory (DFT). Hence, the same energy density functionals (EDFs) obtained from the knowledge of the static properties of nuclei can be applied in dynamic simulations without any further approximation.

With advances of computing capabilities, nowadays one can perform TDDFT simulations that were not possible even twenty years ago. For example, the linear-response properties of medium or heavy nuclei, fission dynamics of actinides, as well as nuclear reaction involving medium-heavy nuclei are within the reach of calculations with single-node computers.

tions with single-node computers.

However, there are still demanding applications. For instance, for the time-dependent Hartree-Fock-Bogoliubov simulations in three-dimensional (3D) real space [12–14], one still needs supercomputers. In the linearized limit, harmonic-oscillator (HO) based time-dependent Hartree-Fock-Bogoliubov (TDHFB) calculations with finite-range Gogny force have become available [15, 16], taking advantage of the fact that the oscillation extends only in a relatively small region. Recently, finite-amplitude method for quasi-particle random-phase approximation (FAM-QRPA) calculations in 3D Cartesian coordinate space have also emerged [17].

It is the purpose of the current work to present a new development, enabling the time-dependent capabilities, based on an earlier DFT code [18]. Currently, the code is represented in 3D Cartesian coordinate space, using a light-weighted finite-difference method for derivative operators. It features an interface with the HFODD code [19–21], which is a Skyrme-Hartree-Fock-Bogoliubov (HFB) code in a 3D coordinate HO basis. Such a flexible code is expected to provide a reasonable alternative for future developments.

As the first application, the current work provides systematic calculations for the isovector (IV) electric dipole

---

\*corresponding author: yueshi@hit.edu.cn

(*E1*) vibration motion for stable and neutron-rich Zr, Mo, and Ru isotopes. Although there exist a few systematic calculations for IV and isoscalar vibrational properties for nuclei across the nuclear chart [22–25], we find that a detailed analysis of the shape evolutions and shape coexistence in the same nucleus, reflected by the different structures of the GDR cross sections, is particularly useful [26].

In Sec. II we present a description about the main features of the current TDDFT framework. Section III contains two parts: first, a set of careful benchmark calculations, with the current TDDFT, Sky3D codes, and the FAM-QRPA calculations, have been presented. Second, systematic calculations have been performed for the photoabsorption cross section of the isovector dipole (IVD) vibration in the spherical and deformed Zr, Mo, and Ru nuclei. A summary is contained in Sec. IV.

## II. THE MODEL

This section describes in detail the procedure for the time development in connection with the previous static calculation [18]. Then, we briefly describe the Sky3D [27] calculation, with which the current code is benchmarked. For the applications in the linearized limit of the current TDDFT calculation, we provide formulae for describing the relevant properties associated with the *E1* vibrational mode.

### A. The static calculations

Before the single-particle wave functions are propagated in time, one has to obtain the static solution of the HF problem. In this stage of the calculation, the time-odd components of the densities and mean-fields vanish for even-even nuclei. The form of the Hamiltonian, the way how the operators of the Hamiltonian are constructed, and how the integrations are performed have been explained in Ref. [18].

#### 1. The grid points arrangement

The grid points in the present implementation are moved away from the origin of the simulating box and differs from those of Ref. [18]. Specifically, in the example of one dimension, instead of using a set of coordinates at

$$[-nx_{\max}, \dots, 0, 1, \dots + nx_{\max}] \times dx, \quad (1)$$

the current code represents the problem on grid points at the coordinates

$$[-nx_{\max} + 0.5, \dots, -0.5, 0.5, \dots + nx_{\max} - 0.5] \times dx, \quad (2)$$

where  $nx_{\max}$  is an integer number numerating the points at the edge of the simulating box. The  $dx$  denotes the

grid spacing. Note, that the latter choice has an even number of grid points, whereas the former one has an odd number of grid points. This choice is guided by the fact that the inclusion of the grid point at the origin of the box results in numerical problems [28]. Using the grid shown in Eq. (2), the integration can be carried out by summation *on* the grid, without the interpolation as presented in Ref. [18].

#### 2. The Bardeen-Cooper-Schrieffer (BCS) pairing

To demonstrate the influence of the pairing interaction on the properties of the IVD resonances, we include a simple BCS pairing [29–31]. For BCS method, we attach each single-particle wave function a real number,  $v_i$ , whose square gives the occupation probability of the  $i$ th orbit.

After each HF iteration, the occupation amplitude  $v_i$  is determined, in the current work, by the following BCS equations

$$v_{i,q}^2 = \frac{1}{2} \left[ 1 - \frac{\epsilon_{i,q} - \lambda_q}{\sqrt{(\epsilon_{i,q} - \lambda_q)^2 + \Delta_{i,q}^2}} \right], \quad (3)$$

where  $\epsilon_{i,q}$ 's are the HF single-particle energies;  $\lambda_q$  is the Fermi energy for given nucleonic type, which is adjusted so that  $2 \sum_i v_{i,q}^2$  gives the correct nucleon number. In Eq. (3), the state-dependent single-particle pairing gaps,  $\Delta_{i,q}$ 's, are given by

$$\Delta_{i,q} = \sum_{\sigma} \int d\mathbf{r} \Delta_q(\mathbf{r}) \psi_{i,q}^*(\mathbf{r}, \sigma) \psi_{i,q}(\mathbf{r}, \sigma), \quad (4)$$

where

$$\Delta_q(\mathbf{r}) = -\frac{1}{2} V_q \int d\mathbf{r} \left[ 1 - \frac{\rho(\mathbf{r})}{\rho_{\text{pair}}} \right] \tilde{\rho}_q(\mathbf{r}), \quad (5)$$

$$\rho_q(\mathbf{r}) = \sum_{i,\sigma} v_{i,q}^2 \psi_{i,q}^*(\mathbf{r}, \sigma) \psi_{i,q}(\mathbf{r}, \sigma), \quad (6)$$

$$\tilde{\rho}_q(\mathbf{r}) = \sum_{i,\sigma} v_{i,q} \sqrt{1 - v_{i,q}^2} \psi_{i,q}^*(\mathbf{r}, \sigma) \psi_{i,q}(\mathbf{r}, \sigma). \quad (7)$$

with  $q = n, p$  denoting the neutron and proton, respectively. The quantities without subscriptions denote the summed contributions from protons and neutrons, for example,  $\rho = \rho_n + \rho_p$ . We choose  $\rho_{\text{pair}} = 0.32 \text{ fm}^{-3}$  in this work.

When applied to the drip-line nuclei, using the BCS pairing tends to scatter the particles to the positive-energy levels which are non-local, resulting in the unphysical nucleon gas surrounding the nucleus. This problem can be cured by replacing the BCS theory with the HFB theory [32].

### B. The nuclear mean fields including the time-odd parts

In the earlier static code presented in Ref. [18], it has been explained that the time-odd densities and mean fields vanish due to the time-reversal symmetry. When time propagation is discussed, the time-odd densities and mean fields appear [1]. Due to computing limitations, historically, the earlier TDHF calculations contained a few serious approximations such as the schematic treatment of the spin-orbit and pairing interactions. Modern TDHF calculations [9–11] include the full Skyrme interactions. Recent studies discuss the influence of the tensor interactions when applied to the description of GDR [33] and nuclear collisions [34].

The current paper adopts the frequently-used Skyrme EDF which contains, in addition to the time-even densities, time-odd densities  $\mathbf{s}$ ,  $\mathbf{j}$ . The tensor interaction is not considered in this work. See Eq. (A.19) of Ref. [1] for a detailed form of the Skyrme energy density  $\mathcal{H}(\mathbf{r})$ .

After variation of the total energy,  $E = \int \mathcal{H}(\mathbf{r}) d\mathbf{r}$ , with respect to the proton and neutron single-particle wave functions, the resulting Skyrme mean fields also contain terms of the above-mentioned time-odd densities. Modern nuclear DFT allows for a free parametrization of coupling constants in front of each term in the Skyrme mean field. See Eq. (2.6) of Ref. [35] for details. Assuming local gauge invariance of the energy density, one requires the terms contributing to the mean fields to be grouped in pairs [35], specifically,  $(\rho\tau - \mathbf{j}^2)$  and  $(\rho\mathbf{\nabla} \cdot \mathbf{J} + \mathbf{s} \cdot \mathbf{\nabla} \times \mathbf{j})$ .

In the current implementation of the TDDFT code, the single-particle Hamiltonian reads

$$\hat{h}_q = -\mathbf{\nabla} \cdot \frac{\hbar^2}{2m^*} \mathbf{\nabla} + U_q - i\mathbf{B}_q \cdot (\mathbf{\nabla} \times \boldsymbol{\sigma}) + \boldsymbol{\sigma} \cdot \boldsymbol{\Sigma}_q + \frac{1}{2i}(\mathbf{\nabla} \cdot \mathbf{I}_q + \mathbf{I}_q \cdot \mathbf{\nabla}). \quad (8)$$

For protons, one needs to add Coulomb potentials [Eqs. (20,24) in Ref. [18]]. The detailed expression of  $U_q$  can be found in Eq. (18) of Ref. [18]. The time-odd potentials included in Eq. (8) read

$$\boldsymbol{\Sigma}_q = \frac{1}{3}(-b_0 + 2b'_0)\mathbf{s} - \frac{1}{3}(2b_0 - b'_0)\mathbf{s}_q - b_4\mathbf{\nabla} \times \mathbf{j} - b'_4\mathbf{\nabla} \times \mathbf{j}_q, \quad (9)$$

$$\mathbf{I}_q = -2b_1\mathbf{j} + 2b'_1\mathbf{j}_q - b_4\mathbf{\nabla} \times \mathbf{s} - b'_4\mathbf{\nabla} \times \mathbf{s}_q. \quad (10)$$

In the EDFs, the term containing  $\mathbf{s} \cdot \Delta\mathbf{s}$  is ignored.

### C. Time propagation

The nuclear non-relativistic time-dependent Schrödinger equation reads

$$i\hbar \frac{\partial \psi_{i,q}(t)}{\partial t} = \hat{h}_q(t) \psi_{i,q}(t), \quad (11)$$

where  $\hat{h}_q$  can be found in Eq. (8). In this section, the subscription  $q$  is ignored for simplicity. The equation (11) has the formal solution

$$\psi_i(t) = \hat{\mathcal{U}}(t) \psi_i(0) = \hat{T} \exp\left(-\frac{i}{\hbar} \int_0^t \hat{h}(t') dt'\right) \psi_i(0), \quad (12)$$

where  $\hat{\mathcal{U}}$  is the time-evolution operator, and  $\hat{T}$  is the time-ordering operator. To solve the time-dependent problem, one breaks up the total time evolution into  $N$  small increments of time  $\Delta t$

$$\hat{U}(t, t + \Delta t) = \exp\left(-\frac{i}{\hbar} \int_t^{t+\Delta t} \hat{h}(t') dt'\right). \quad (13)$$

The time-evolution operator  $\hat{\mathcal{U}}(t)$  can be obtained by consecutive actions of  $\hat{U}(t, t + \Delta t)$

$$\hat{\mathcal{U}}(t) = \prod_{n=0}^{N-1} \hat{U}(n\Delta t, (n+1)\Delta t). \quad (14)$$

For small  $\Delta t$  one could approximate  $\hat{U}(t, t + \Delta t)$  by Taylor expansion up to order  $m$ :

$$\exp\left(-\frac{i}{\hbar} \hat{h} \Delta t\right) \approx \sum_{n=0}^m \frac{1}{n!} \left(-\frac{i\Delta t}{\hbar}\right)^n \hat{h}^n, \quad (15)$$

where  $\hat{h}$  has been assumed to be time independent in the time interval of  $\Delta t$ . In the current work,  $\Delta t$  is taken to be 0.2 fm/c, and  $m = 4$ . These choices are motivated by previous TDHF calculations.

In the realistic calculations, each time advance of single-particle wave functions  $\psi_i$ , from time  $t$  to  $t + \Delta t$ , has been achieved by using the Crank-Nicholson method [2]. Specifically, from a series of single-particle wave functions at  $t$ ,  $\psi_i(t)$ , one first performs

$$\psi_i^{\text{temp}}(t + \Delta t) = \hat{U}^t(t, t + \Delta t) \psi_i(t). \quad (16)$$

Having  $\psi_i^{\text{temp}}(t + \Delta t)$ , and  $\psi_i(t)$ , one assembles various densities using respective single-particle wave functions, obtaining the  $\rho^{\text{temp}}(t + \Delta t)$  and  $\rho(t)$ .

Using these densities, one obtains the densities at a “middle time”,  $\rho^{\text{mid}}(t + \frac{\Delta t}{2}) = 0.5[\rho^{\text{temp}}(t + \Delta t) + \rho(t)]$ . Now, one constructs the Hamiltonian  $\hat{h}^{\text{mid}}$ , using  $\rho^{\text{mid}}(t + \frac{\Delta t}{2})$  [see Eq. (15) of Ref. [18], and Eq. (8) for the form of the Hamiltonian]. A second time propagation operation  $\hat{U}^{\text{mid}}(t, t + \Delta t)$  with  $\hat{h}^{\text{mid}}$  [Eq. (15)] is performed on the single-particle levels, finally obtaining the wave functions at  $t + \Delta t$

$$\psi_i(t + \Delta t) = \hat{U}^{\text{mid}}(t, t + \Delta t) \psi_i(t). \quad (17)$$

Here,  $\hat{U}^{\text{mid}}$  differs from  $\hat{U}^t$  [Eq. (16)] in that the former uses the single-particle Hamiltonian in its exponent [Eq. (15)] at the time  $t + \frac{\Delta t}{2}$ , whereas the latter refers

to the operator  $\hat{U}$ , where the Hamiltonian is constructed using the quantities at the time  $t$ .

Note that in the above procedure, one has to perform the time propagation twice. The single-particle Hamiltonian does not contain time specifically. In realistic calculations, the unitarity of the operator  $\exp\left(-\frac{i}{\hbar}\hat{h}\Delta t\right)$  needs to be checked as it is approximated using a Taylor expansion [Eq. (15)]. For the chosen parameter,  $\Delta t = 0.2 \text{ fm}/c$  and  $m = 4$ , we evaluate the matrix elements

$$\mathcal{I}_{ij} \equiv \langle \psi_i(t) | \hat{U} | \psi_j(t) \rangle \approx \langle \psi_i(t) | \psi_j(t + \Delta t) \rangle. \quad (18)$$

Both the diagonal and off-diagonal matrix elements start to deviate from 1 and 0, respectively, at or after the 6th place after the decimal point. For a better approximation of the  $\hat{U}$  operator, one could decrease  $\Delta t$  and increase  $m$ .

When the BCS pairing is included, the occupation amplitudes,  $v_{i,q}$ 's in Eq. (3), are kept unchanged when calculating the densities during the time development. When evaluating the densities, the single-particle wave functions vary according to Eq. (11). This is a coarse approximation of dynamical pairing, as the occupation probabilities should vary with time. A natural solution would be to solve the full time-dependent HFB problem [12–14]. Since the HFB theory treats nuclear interactions in the particle-hole and pairing channels in one single variational process [30], a time-dependent HFB treatment allows for the occupation amplitudes being determined dynamically by the upper and lower components at a given time. In 3D Cartesian coordinate space, such methods require a direct diagonalization of a large HFB matrix. Work in this direction is in progress.

#### D. Absorbing boundary conditions (ABC)

With Dirichlet boundary conditions, it has been known that the TDDFT calculations show the occurrence of non-physical particle densities at the boundary region. To cure this problem, it has been proposed [9] to use the so-called absorbing boundary conditions. This is achieved by introducing an imaginary potential

$$\hat{h}(\mathbf{r}) \rightarrow \hat{h}(\mathbf{r}) + i\tilde{\eta}(\mathbf{r}) \quad (19a)$$

at the boundary region of the form

$$\tilde{\eta}(\mathbf{r}) = \begin{cases} 0 & \text{for } 0 < |\mathbf{r}| \leq R \\ \eta_0 \frac{|\mathbf{r}| - R}{\Delta r} & \text{for } R < |\mathbf{r}| < R + \Delta r \end{cases} \quad (19b)$$

Recently, there have been efforts using more involved boundary conditions [36, 37]. Based on these studies, we decide to use the ABC due to its simplicity and effectiveness.

#### E. IVD resonance calculations

The IVD resonance is the most common vibrational mode in nuclear physics, where protons and neutrons vibrate against each other. This mode is responsible for the

$E1$  resonant strengths in the energy range of  $\sim 10$ – $20$  MeV. This broad peak is called giant dipole resonance (GDR) [38]. The current work aims at a description of the IVD resonance in terms of the TDDFT in its linearized limit, which is equivalent to the random-phase approximation (RPA) [30].

In the TDDFT description, the strength of this IVD vibrational mode can be obtained by applying the following small boost on the obtained single-particle wave functions,

$$\psi_{i,q}(\mathbf{r}, \sigma; t = 0+) \equiv \exp \left[ -i\epsilon \sum_{\mu=-1}^{+1} \mathcal{M}(E1, \mu) \right] \psi_{i,q}(\mathbf{r}, \sigma), \quad (20)$$

with the IV operator  $\mathcal{M}(E1, \mu)$  defined as

$$\mathcal{M}(E1, \mu) = e_q^{(E1)} r Y_{1\mu}(\hat{\mathbf{r}}) \quad \mu = 0, \pm 1, \quad (21)$$

where  $e_p^{(E1)} = Ne/A$ , and  $e_n^{(E1)} = -Ze/A$ . When  $\mathcal{M}(E1, \mu)$  acts on proton/neutron single-particle wave functions, its coefficient takes value of  $e_p^{(E1)}/e_n^{(E1)}$ . The real spherical harmonics are defined as

$$\{Y_{1\mu}\}_{\mu=-1,0,1} = \left\{ \sqrt{\frac{3}{4\pi}} \frac{\lambda}{r} \right\}_{\lambda=y,z,x}. \quad (22)$$

In Eq. (20), the boosted single-particle wave functions differ from the static ones by including “ $t = 0+$ ”, indicating their time-dependency. This IV boost has to be small enough to ensure that the vibration is still within the linearized regime. The typical magnitude of  $|\epsilon|$  is  $10^{-3} (e \text{ fm})^{-1}$ . In this work, we apply 3D boost which has been indicated by the summation over  $\mu$  in the exponent in Eq. (20). The boost is applied over the whole box, although a masking procedure works better confining its effect in the range of the nucleus [39].

The time evolution of the dipole moment

$$\langle \mathcal{M}(E1, \mu) \rangle \equiv \int e_n^{(E1)} \rho_n r Y_{1\mu} d\mathbf{r} + \int e_p^{(E1)} \rho_p r Y_{1\mu} d\mathbf{r} \quad (23)$$

is then recorded to certain length of time. The strengths are the Fourier transform of  $\langle \mathcal{M}(E1, \mu) \rangle(t)$

$$S(E; E1) = -\frac{1}{\pi \hbar \epsilon} \text{Im} \sum_{\mu=-1}^{+1} \int \langle \mathcal{M}(E1, \mu) \rangle(t) dt e^{(iE - \Gamma/2)t/\hbar}, \quad (24)$$

where  $\Gamma$  is a smoothing parameter. The photoabsorption cross section associated with the IVD resonance is obtained as follows [40, 41]

$$\sigma_{\text{abs.}} = \frac{4\pi^2}{\hbar c} E \times S(E; E1). \quad (25)$$

#### F. Calculation of energy-weighted sum rule (EWSR) for the IVD vibration

Another important aspect of the vibration calculations is the evaluation of EWSR [30], which is a useful check of

the implementation of the TDDFT code. In the TDDFT code, the sum rule is calculated using

$$m_1 = \int E \times S(E; E1) dE. \quad (26)$$

Recently, the EWSR for the density functional theory has been systematically derived in Refs. [42, 43]. For the current IVD operator, the sum rule using Eq. (98) of Ref. [43] can be adapted as follows

$$\begin{aligned} m_1 = & \sum_{\mu=-1}^{+1} \int d\mathbf{r} [\nabla(rY_{1\mu})]^2 \left\{ \frac{\hbar^2}{2m} [e_n^{(E1)^2} \rho_n + e_p^{(E1)^2} \rho_p] \right. \\ & + (C_0^\tau - C_1^\tau) (e_n^{(E1)} + e_p^{(E1)})^2 \rho_n \rho_p \\ & \left. + \sum_{k=0,1} (C_k^\tau - C_k^j) [e_n^{(E1)} \rho_n + (-1)^{k+1} e_p^{(E1)} \rho_p]^2 \right\}. \quad (27) \end{aligned}$$

The definition of the spherical harmonics can be found in Eq. (21). The coupling constants in terms of  $C_{0,1}^{\tau,j}$  are related to  $b_1, b'_1$  through

$$C_0^\tau = -C_0^j = b_1 - 0.5b'_1, \quad (28)$$

$$C_1^\tau = -C_1^j = -0.5b'_1. \quad (29)$$

If we define the kinetic-energy contribution

$$\begin{aligned} m_1^{\text{kin}} = & \sum_{\mu=-1}^{+1} \int d\mathbf{r} [\nabla(rY_{1\mu})]^2 \frac{\hbar^2}{2m} [e_n^{(E1)^2} \rho_n + e_p^{(E1)^2} \rho_p] \\ = & \frac{9}{4\pi} \frac{\hbar^2}{2m} \frac{NZ}{A} e^2, \quad (30) \end{aligned}$$

then the enhancement factor,  $\kappa$ , due to the contribution of interaction-energy term with respect to the kinetic part, can be calculated through

$$m_1 = m_1^{\text{kin}} (1 + \kappa). \quad (31)$$

The classical sum rule of the IVD operator, which is the Thomas-Reiche-Kuhn (TRK) sum rule [44] can be analytically expressed as shown in Eq. (30).

The EWSR value obtained from Eq. (27) are related to various densities of the ground state. Thus, they can be determined rather precisely. To what extent the  $m_1$  values obtained from TDDFT [Eq. (26)] and Eq. (27) agree, forms a stringent testing ground for the TDDFT code.

### G. Sky3D calculations

To demonstrate the precision of the current code, it is necessary to benchmark it against an existing code with an identical calculation. In this work, this benchmark is done with a well established code Sky3D.

We use the Sky3D code as described in Refs. [27, 28]. An important difference to the implementation presented

in this code is that derivatives are performed utilizing the fast Fourier transform and thus the natural boundary conditions are periodic boundary conditions. The difference is of special importance for time-dependent calculations, as it affects the quantization of unbound energy states. Furthermore, when evaporated material is leaving the box it is again introduced from the other side of the box and not reflected as with Dirichlet boundary conditions. The codes differ slightly in the way the density at middle time is approximated. In Sky3D the wave functions are propagated until middle time  $t + \Delta t/2$ . These densities are then directly taken to calculate the Hamiltonian at middle time  $\hat{h}^{\text{mid}}$ .

For the benchmarks we implemented the same boost as described in Sec. II E and also the imaginary potential for ABC from Sec. II D.

## III. CALCULATED RESULTS

To complete the benchmark of the implemented TDDFT code, one has to include careful calculations and compare the calculated results with those of existing codes. The particularly useful testing cases for the TDDFT code is the calculation of IVD resonance for light spherical and deformed nuclei.

In Ref. [9] careful comparative study has been done between the TDDFT code and the RPA calculations. Detailed dipole-moment response as a function of time, as well as the corresponding strengths results for  $^{16}\text{O}$  nucleus has been presented with the specific force being provided. In this section, we first present results of the current code, comparing them with those of Sky3D code and Ref. [9]. The calculation is then extended to spherical nucleus  $^{40}\text{Ca}$ , as well as deformed magnesium isotopes  $^{24,34}\text{Mg}$  with conventional Skyrme EDF SkM\* [45], and a more recent EDF UNEDF1 [46].

The UNEDF1 EDF contains Lipkin-Nogami (LN) pairing [46] in the parameter adjustment process. In principle, one has to include this part specifically. However, we decide to be more flexible in the pairing treatment for the current TDDFT calculations based on two considerations. First, the original UNEDF1 parameter is determined in the HO basis and with specific cut-off on the Hartree-Fock-Bogoliubov problem. Whereas the current code is working in Cartesian coordinate space. Hence, the continuum is discretized differently from that of a HO code. Consequently, there is no way to make the pairing treatment identical in the two codes [18]. Second, the observables we are interested in, namely, the strengths for IVD resonances are well known to be insensitive to pairing interactions [47]. The strengths corresponding to pygmy dipole resonance (PDR) are only enhanced very marginally by including the pairing interaction, as will be shown in Sec. III A 3.

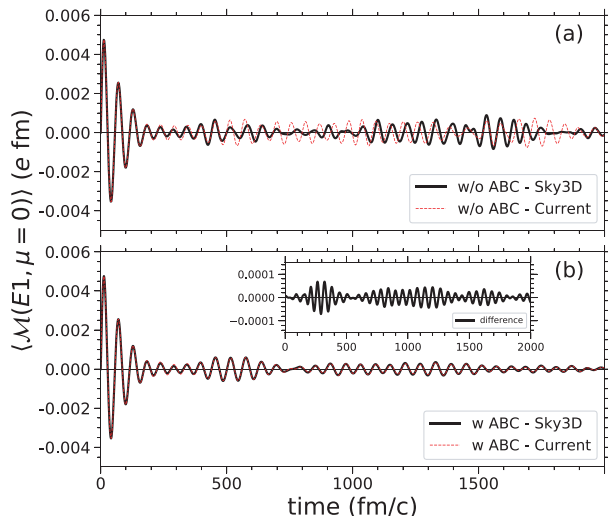


FIG. 1: The responses of  $\langle \mathcal{M}(E1, \mu = 0) \rangle(t)$  of  $^{16}\text{O}$  calculated with the current TDDFT code and the Sky3D code [28]. The inset of panel (b) shows the difference between the  $\langle \mathcal{M}(E1, \mu = 0) \rangle$  values of the TDDFT and the Sky3D results.

### A. Results for light nuclei

#### 1. Benchmark calculations for $^{16}\text{O}$ with Skyrme SIII EDF

The nucleus  $^{16}\text{O}$  is of particular interest in theoretical benchmarking calculations, as the structure of the strength is sensitive to the included terms in the EDF [9]. Hence, many theoretical methods [33, 48, 49] took  $^{16}\text{O}$  as a testing case for the proposed method. In this section, we perform TDDFT calculations with Skyrme force parameter SIII [50] with time-odd potentials in the form of Eq. (9) (SIII-full), as well as SIII without any time-odd contributions (SIII-even).

Figure 1 displays a set of comparisons of responses of dipole moments between the currently implemented code and the Sky3D code. In these calculations, the time-odd potentials are identical with that of the Sky3D code [Eqs. (8e,8f) of Ref. [28]]. Specifically, the time-odd potentials are in the form of Eq. (9), except that the terms including *only s* are left out.

Figure 1(a) compares the response functions without any absorbing mechanism. We see that the magnitude agrees well for  $t \leq 400$  fm/c. However, the good agreement starts to deteriorate after  $t \approx 500$  fm/c. This is due to the different boundary conditions used in the two codes, which results in the different treatment of the particle densities bounced back from the border of the box. Indeed, even within the same code, using a finer grid results in rather different response functions after certain time.

Figure 1(b) compares the response functions with the ABC [Eq. (19)] calculated with both codes. For both codes we use  $\eta_0 = 10$  MeV,  $R = 10$  fm, and  $\Delta r = 12$  fm. It can be seen that with the same ABC, both codes give

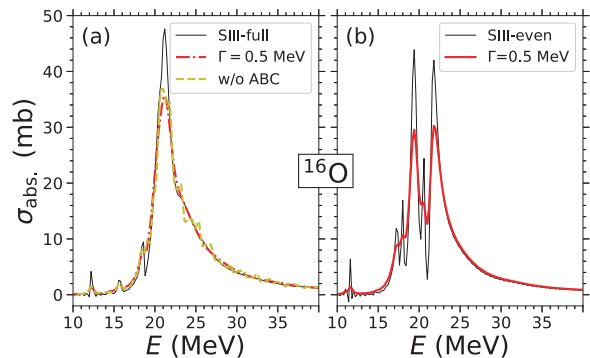


FIG. 2: The calculated photoabsorption cross sections of  $^{16}\text{O}$  using Eq. (25). The left panel shows the results with SIII-full EDF, whereas the right panel shows those of SIII-even. The thinner black lines indicate results without smoothing procedure.

almost identical response functions. The difference of the dipole moment, shown in the inset, is at least an order of magnitude smaller than the original moment value. The agreement is remarkable. Indeed, one has to take into account the fact that there are many differences in the features as discussed in Sec. II G.

Figure 2 shows the photoabsorption cross sections calculated with Eq. (25) for SIII-full and SIII-even, with  $\Gamma = 0.5$  MeV and without the smoothing procedure ( $\Gamma = 0$ ). Again, a good correspondence can be seen between Fig. 6(b) of Ref. [9] and Fig. 2 of the current work. Specifically, for SIII-full we see, for both results, that the single largest peak occurs at  $E \approx 21.2$  MeV. For SIII-even, the two peaks occur at  $E \approx 19.4$  and  $21.8$  MeV for both the current result and those shown in Fig. 6(b) of Ref. [9]. Using a smoothing parameter of  $\Gamma = 0.5$  MeV brings the general shape of the curves rather close to those given in Fig. 6(b) of Ref. [9]. It has to be noted that the peak heights of the cross section curves in the current work differ from those shown in Ref. [9] by  $\sim 10$  mb.

In these calculations, we use the ABC as described in Sec. II D. In Fig. 2(a), we also include the results without the ABC. It can be seen that the strength without the ABC differs from that with the ABC in that the former gives small peaks for excitation energies larger than that corresponding to the main peak. These small peaks are spurious which are removed by absorbing potential in the outer layer region.

#### 2. Comparing TDDFT with FAM-QRPA: $^{16}\text{O}$ and $^{40}\text{Ca}$

In this section, we compare our TDDFT approach to the QRPA calculation based on the linear-response formalism, the finite-amplitude method (FAM) [51, 52]. The FAM allows us to calculate the response function without constructing the QRPA matrices in the case of the nuclear DFT. The present implementation of the FAM-QRPA [53] is based on the nuclear DFT solver HF-

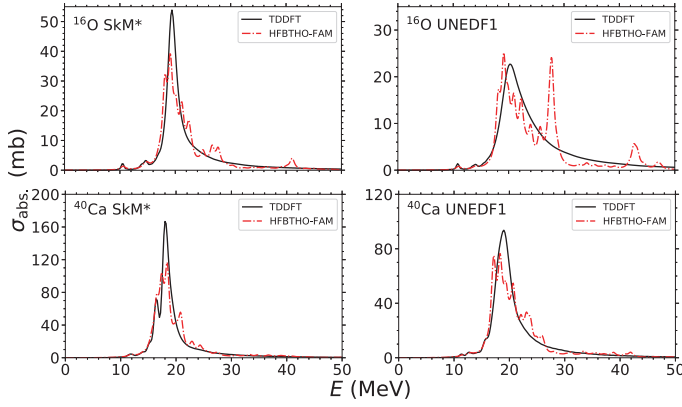


FIG. 3: The calculated photoabsorption cross sections for  $^{16}\text{O}$  and  $^{40}\text{Ca}$ , using TDDFT of the present implementation and FAM-QRPA based on the HFBTHO with the SkM\* and UNEDF1 EDFs.

BTHO [54–56], which allows to describe the superconducting axially deformed nuclei in the HO basis.

Before showing the cross-section results, we first present the calculated static properties using both codes. Table I lists the calculated ground-state energy decomposition into various terms, as well as the root-mean-square radii. For a fixed box size, three different grid spacings have been used. It can be seen that the ground-state energy is overbound by  $<200$  keV using the coarsest grid with  $dx = 1.0$  fm. Using finer grid spacings reduces the total energy differences to  $\leq 50$  keV. It should be noted that, the seemingly poor accuracy of a spacing of 1.0 fm does not drastically affect the dynamic calculation [see Fig. 1(b)].

Figure 3 shows the photoabsorption cross sections for  $^{16}\text{O}$  and  $^{40}\text{Ca}$  calculated with the TDDFT and FAM-QRPA. The energy of the main peak and the low-energy side of the main peak agree well between the two approaches, while the high-energy tail part is more fragmented in the FAM-QRPA strength. This behavior found in the calculation using the HO basis is also found in the QRPA calculations in deformed nuclei using the HO basis [57, 58].

Figure 4 displays the HFBTHO-FAM results with increasing number of HO basis ( $N_{\text{sh}}$ ). We see that the peak at  $E \sim 25\text{--}35$  MeV moves toward the main peak with increasing  $N_{\text{sh}}$ . We note a slow convergence of the strength function for this nucleus with this particular EDF. For medium-heavy nuclei, the isoscalar and isovector multipole strength functions are found to be converged already at  $N_{\text{sh}} = 20$  [41, 59].

### 3. Results for deformed nuclei: $^{24,34}\text{Mg}$

The nucleus  $^{24}\text{Mg}$  is one of the lightest nuclei with large prolate deformation. Hence, the IVD vibration motion of this nucleus has been frequently used as a testing case for TDDFT or RPA codes. Another interesting system

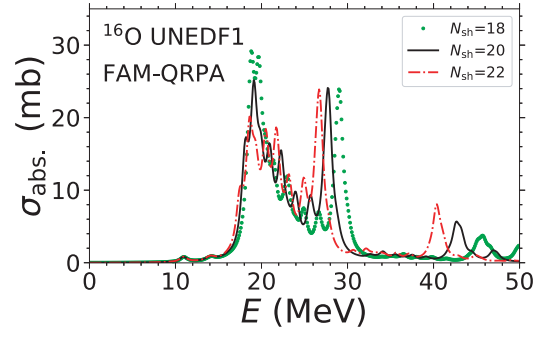


FIG. 4: The calculated photoabsorption cross sections for  $^{16}\text{O}$ , using HFBTHO-FAM method with the UNEDF1 EDF. Three different HO basis numbers are used to see the convergence of the results.

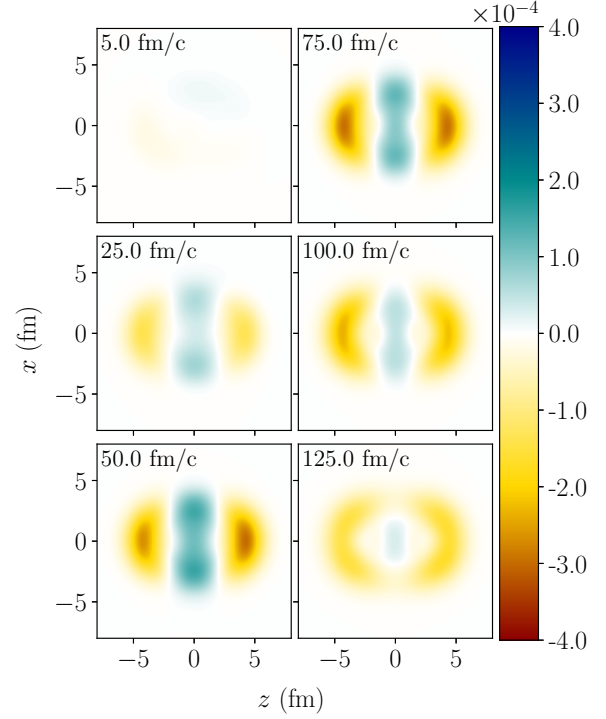


FIG. 5: Evolution of the IV density  $\rho_p(\mathbf{r}) - \rho_n(\mathbf{r})$  (in  $\text{fm}^{-3}$ ) in the  $x - z$  plane ( $y = 0$ ) for the IVD mode in  $^{24}\text{Mg}$ .

that has a prolately deformed ground state is  $^{34}\text{Mg}$ . The occurrence of non-zero strength below  $E = 10$  MeV in  $^{34}\text{Mg}$  is a signature of the pygmy mode for neutron-rich Mg isotopes [60]. For neutrons, there is a pairing correlation which makes  $^{34}\text{Mg}$  particularly interesting. In this section, we focus on the description of  $^{24,34}\text{Mg}$  with both TDDFT and the HFBTHO-FAM methods.

Table II lists the calculated static information on  $^{24}\text{Mg}$  with SkM\* and UNEDF1 EDFs. Figure 5 plots the IV densities,  $\rho_p(\mathbf{r}) - \rho_n(\mathbf{r})$ , on the  $x - z$  plane with  $y = 0$ , at a few instances. As the protons and neutrons vibrate against each other, a fading and strengthening pattern of the color can be seen. Careful examination reveals the



TABLE I: The calculated static properties for  $^{16}\text{O}$  and  $^{40}\text{Ca}$  with UNEDF1 EDF, using TDDFT and HFBTHO codes. For the TDDFT calculations, the simulation boxes have dimensions of  $[-14.5, +14.5]^3 \text{ fm}^3$ . Three grid spacings have been used to see the convergence of the TDDFT calculations. For the HFBTHO calculations, 20 HO shells are used.

	$^{16}\text{O}$				$^{40}\text{Ca}$			
	Current			HFBTHO	Current			HFBTHO
	$\Delta x=1.0 \text{ fm}$	$\Delta x=0.784 \text{ fm}$	$\Delta x=0.707 \text{ fm}$		$\Delta x=1.0 \text{ fm}$	$\Delta x=0.784 \text{ fm}$	$\Delta x=0.707 \text{ fm}$	
$E_{\text{tot}}$ (MeV)	-121.139	-120.997	-120.986	-121.000	-340.873	-340.599	-340.571	-340.625
$E_{\text{Kin.}}$ (MeV)	236.905	236.443	236.414	236.494	659.414	658.387	658.290	658.505
$E_{\rho}$ (MeV)	-406.666	-405.978	-405.936	-406.055	-1137.525	-1135.918	-1135.749	-1136.071
$E_{\tau}$ (MeV)	-0.890	-0.886	-0.886	-0.886	-3.218	-3.209	-3.207	-3.209
$E_{\Delta\rho}$ (MeV)	36.522	36.486	36.492	36.520	68.788	68.601	68.575	68.640
$E_{\text{SO}}$ (MeV)	-0.636	-0.671	-0.677	-0.681	-0.979	-1.046	-1.059	-1.077
$E_{\text{dir.}}^{\text{Coul.}}$ (MeV)	16.448	16.429	16.427	16.428	80.201	80.132	80.124	80.134
$E_{\text{exc.}}^{\text{Coul.}}$ (MeV)	-2.823	-2.820	-2.820	-2.820	-7.554	-7.547	-7.546	-7.548
$r_{\text{rms}}^{\nu}$ (fm)	2.666	2.669	2.669	2.668	3.360	3.362	3.362	3.362
$r_{\text{rms}}^{\pi}$ (fm)	2.684	2.687	2.687	2.686	3.395	3.398	3.398	3.398
$r_{\text{rms}}^{\text{tot.}}$ (fm)	2.675	2.678	2.678	2.677	3.377	3.380	3.380	3.380

TABLE II: Calculated static DFT results for  $^{24}\text{Mg}$  using SkM\* and UNEDF1 EDFs. A comparison is made between the results using the current code and the HFBTHO code [54, 55]. There is no center-of-mass correction for UNEDF1 calculations. The quadrupole moments are defined as  $Q_{20} = 2 \langle \hat{z}^2 \rangle - \langle \hat{x}^2 \rangle - \langle \hat{y}^2 \rangle$ . The single-particle levels are doubly degenerate labeled by  $\Omega^{\text{parity}}$ , where  $\Omega$  denotes the total angular momentum projection of the level onto the  $z$ -axis. All quantities are in units of MeV, except for  $Q_{20}$  values which are in barn.

	SkM*		UNEDF1	
	Current	HFBTHO	Current	HFBTHO
$E_{\text{tot}}$	-197.123	-197.155	-189.881	-189.852
$E_{\text{Kin.}+\text{c.m.}}$	384.483	384.091	401.148	400.387
$E_{\text{Coul}}$	28.681	28.650	28.713	28.671
$E_{\text{Skyrme}}$	-610.287	-609.896	-619.742	-618.910
$Q_{20}$	1.072	1.072	1.126	1.137
$\epsilon_{1/2+}^{\pi}$	-34.236	-34.249	-29.474	-29.480
$\epsilon_{1/2-}^{\pi}$	-23.510	-23.528	-20.865	-20.898
$\epsilon_{3/2-}^{\pi}$	-19.429	-19.396	-17.348	-17.285
$\epsilon_{1/2-}^{\pi}$	-13.945	-13.973	-13.219	-13.196
$\epsilon_{1/2+}^{\pi}$	-12.066	-12.075	-11.036	-11.064
$\epsilon_{3/2+}^{\pi}$	-9.525	-9.519	-8.596	-8.585
$\epsilon_{1/2+}^{\nu}$	-39.279	-39.290	-34.215	-34.218
$\epsilon_{1/2-}^{\nu}$	-28.361	-28.377	-25.500	-25.529
$\epsilon_{3/2-}^{\nu}$	-24.274	-24.235	-22.034	-21.964
$\epsilon_{1/2-}^{\nu}$	-18.667	-18.694	-17.833	-17.806
$\epsilon_{1/2+}^{\nu}$	-16.725	-16.729	-15.604	-15.626
$\epsilon_{3/2+}^{\nu}$	-14.141	-14.131	-13.148	-13.132

left-right and up-down asymmetry, which is due to the 3D boost that has been initiated in the current calculations.

Figure 6 compares the strengths calculated with SkM\* and UNEDF1 EDFs. It can be seen that the two peaks calculated with UNEDF1 EDF are considerably lower and broader compared to those calculated with SkM\* EDF. The positions of the two peaks are a few hundreds of keV higher for UNEDF1 EDF compared to those of SkM\*

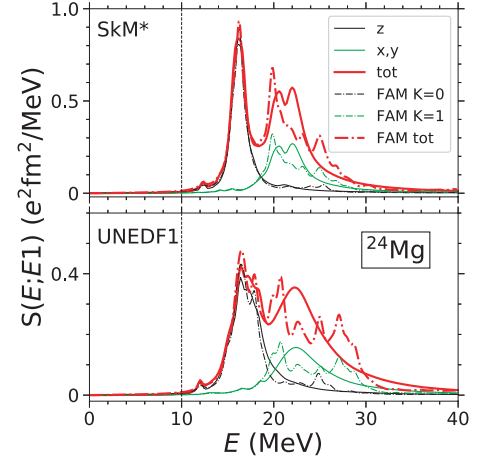


FIG. 6: The calculated strength functions of  $^{24}\text{Mg}$  using SkM\* and UNEDF1 EDFs, with TDDFT and HFBTHO-FAM methods.

EDF. In Fig. 6, we plot our HFBTHO-FAM results too. The strength functions are almost identical up to the first peak, after which the FAM-QRPA calculations show more fragmented second peak or sub-peaks compared to the TDDFT calculations.

For the strength function of  $^{24}\text{Mg}$  calculated with SkM\* EDF, there are a few calculations using different models. For example, in Ref. [48], the photoabsorption cross section for  $^{24}\text{Mg}$  has been calculated with the FAM-QRPA method. In Ref. [60] a canonical-basis TDHF calculation is performed to calculate the  $E1$  strength in  $^{24}\text{Mg}$ . In particular, the result is consistent with their FAM-QRPA results [60]. In Ref. [58], the QRPA calculations using (transformed) HO basis has been performed for the  $E1$  strengths in  $^{24}\text{Mg}$ .

Comparing these three existing results [Fig. 8(g) of Ref. [48], Fig. 2 of Ref. [60], and Fig. 15 of Ref. [58]] with that in the current work which is shown in Fig. 6, it



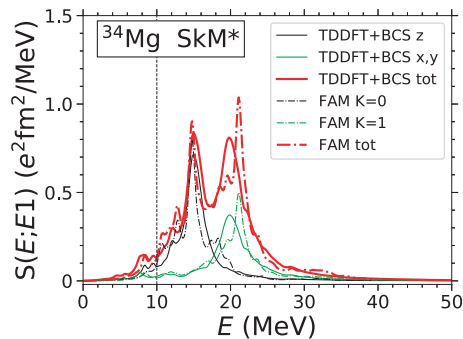


FIG. 7: The calculated strength functions of  $^{34}\text{Mg}$  with SkM\* EDF using TDDFT and FAM-QRPA methods.

can be summarized that, for all calculated results, there are unambiguously two peaks at  $E \approx 16$  and  $22$  MeV. The structure or sub-peaks appearing between these two are susceptible to, presumably, either the box size, or the truncation in the single-particle levels, and HO shells used by the respective models. It is rewarding to see such a consistency among independent methods and implementations.

Figure 7 shows the calculated  $E1$  strengths for  $^{34}\text{Mg}$  using both TDDFT+BCS and the FAM-QRPA calculations. For the TDDFT+BCS calculations, pairing exists only for neutrons. The pairing strength for neutrons is  $V_n = -500 \text{ MeV fm}^3$ . There are 44 single-neutron levels included in the BCS problem. The highest-energy single-particle level has  $\epsilon = 3.85$  MeV. To make the two methods comparable, we have fine tuned the pairing strengths in the HFBTHO calculation in such a way that both codes give similar pairing energies in the static calculations.

We see from Fig. 7 that both calculations yield two peaks at  $E \approx 15$  and  $20$  MeV. Again, the second peak from FAM-QRPA calculation is slightly more fragmented compared to the TDDFT+BCS calculations. These results are consistent with the canonical-basis TDHFB results of Ref. [60].

For the neutron-rich oxygen, neon, and magnesium isotopes, the appearance of the  $E1$  strength below  $E = 10$  MeV are of particular interest [60–62], as they correspond to the pygmy mode of vibration. It has been shown [60] that the inclusion of pairing correlation would result in a small enhancement of the fraction of the strengths below  $E_c = 10$  MeV, compared to a TDDFT result.

We compute the following PDR fraction [25, 60]

$$f_{\text{PDR}} = \frac{m_1(E_c)}{m_1} \equiv \frac{\int^{E_c} E \times S(E) dE}{\int E \times S(E) dE}, \quad (32)$$

for the strength functions from TDDFT calculations with and without pairing. The  $f_{\text{PDR}}$  value is 2.3% for the  $E1$  strength without pairing. When pairing is included, this quantity increases to 2.7%, which is consistent with the results in Ref. [60].

#### 4. Calculated EWSR

Table III compares the  $m_1$  values calculated with the ground-state expectation value [Eq. (27)], and those calculated with the strength function obtained from the TDDFT method [Eq. (26)]. We see that the  $m_1$  values from TDDFT and those from Eq. (27) are rather close. The TDDFT values are systematically smaller than those of Eq. (27) by less than 1% of the  $m_1$  values. This indicates the correctness and good precision of the current implementation of the TDDFT code.

The classical TRK sum-rules [Eq. (30)] are 59.2, 148.0, and 88.8  $e^2 \text{ fm}^2 \text{ MeV}$  for  $^{16}\text{O}$ ,  $^{40}\text{Ca}$ , and  $^{24}\text{Mg}$ , respectively. We have computed the enhancement factor  $\kappa$  using Eq. (31), which are roughly 0.15 and 0.30 for each nucleus using UNEDF1 and SkM\* EDFs, respectively.

TABLE III: The EWSR values of the IVD operator (in  $e^2 \text{ fm}^2 \text{ MeV}$ ) calculated using the current TDDFT code, compared to the ground-state values.

	TDDFT	g.s. value
$^{16}\text{O}$ (SIH-even)	67.1	67.3
$^{16}\text{O}$ (SIH-full)	75.0	75.3
$^{16}\text{O}$ (SkM*)	72.5	72.8
$^{16}\text{O}$ (UNEDF1)	67.0	67.6
$^{40}\text{Ca}$ (SkM*)	194.0	194.9
$^{40}\text{Ca}$ (UNEDF1)	171.4	172.8
$^{24}\text{Mg}$ (SkM*)	113.7	114.3
$^{24}\text{Mg}$ (UNEDF1)	101.8	102.9

#### B. Results for Zr, Mo, and Ru nuclei

In the previous TDDFT calculations for light spherical and deformed nuclei, we have seen the usefulness of the newly developed code. In this section, we perform systematic calculations for the photoabsorption cross sections of Zr, Mo, and Ru nuclei.

##### 1. Results for spherical Zr and Mo isotopes

Spherical Zr and Mo isotopes are interesting systems to study because the experimental cross sections for IVD  $E1$  resonances are available [63, 64]. In particular, for  $^{92-100}\text{Mo}$ , the strengths below the neutron emission threshold have been observed [65–67].

Figure 8 displays the calculated photoabsorption cross sections for Zr and Mo isotopes for which experimental data exists for comparison. In these calculated strengths [Eq. (24)], a relatively larger smoothing parameter,  $\Gamma = 2.0$  MeV, has been used. This is motivated by the observation in a previous RPA calculation [26, 68], where a 2.0 MeV smoothing parameter was seen to produce reasonable descriptions for these cross-section data. Using a smaller smoothing parameter results in the peaks

being more pronounced, and narrower. The centroids remain at the same position. In these TDDFT calculations, we do not include BCS pairing since the relevant observables associated with the IVD resonances are insensitive to pairing.

We see from Fig. 8 that both the widths and the centroid of the GDR peak are well reproduced by the current TDDFT calculations. For Mo isotopes, the low-energy part ( $E \leq 10$  MeV) of the cross section were observed using bremsstrahlung method [65–67]. In the third row of Fig. 8, the same cross sections for Mo isotopes are plotted in a logarithmic scale. Our calculated results well reproduce the low-energy part ( $E < 10$  MeV) of the experimental data, especially for  $^{96-100}\text{Mo}$ .

Note that the linear-response theories, such as those adopted in the current work, contain correlations on the one-particle-one-hole (1p-1h) level. To fully account for the width of the GDR peak, it is important to include 2p-2h correlations [38]. It is satisfactory to see that the positions of the centroids, and the general structures of the GDR peaks are reasonably well reproduced.

## 2. Static potential energy surfaces for neutron-rich nuclei

The shape evolution of the ground states of neutron-rich zirconium isotopes are particularly interesting, with prolate and oblate minima competing to become ground states [71, 72]. With recent advances in the rare isotope facilities, the interesting low-energy spectra for the most neutron-rich isotopes in the Zr, Mo, and Ru nuclei [73–76] are becoming more and more available. From various models, the neutron-rich isotopes of Mo and Ru are calculated to have well-defined triaxially deformed ground states [77–79].

Before showing the calculated IV  $E1$  photoabsorption cross section of these neutron-rich nuclei, it is necessary to have some idea about the potential-energy surfaces of quadrupole deformations. Figures 9, 10, and 11 display the potential-energy surfaces for even-even  $^{98-108}\text{Zr}$ ,  $^{100-110}\text{Mo}$ , and  $^{102-112}\text{Ru}$  nuclei, calculated with UNEDF1 EDF. The constraint HFB calculations for these potential-energy surfaces are performed with the HFODD code (version 2.68h). For these HFB+LN calculations, there are 1140 ( $N = 17$ ) spherical HO bases included; the original pairing strengths and energy cut-off on the quasi-particle spectra are used [46].

For the Zr isotopes, the spherical ground states for  $50 \leq N \leq 58$  are replaced by a situation where prolate and oblate minima coexist for  $^{100,102}\text{Zr}$ , with the prolate minimum being slightly lower energetically in  $^{102}\text{Zr}$ . For Zr isotopes with  $N \geq 64$ , the prolate minima move to a static triaxial deformation, with the oblate minima staying slightly higher in energy.

For Mo and Ru isotopes with  $N \geq 60$ , the ground states are dominated with a triaxial deformation. For all Mo isotopes, the shape is rather soft in the  $\gamma$  direction. Whereas for the Ru isotopes, the  $\gamma$ -deformation is more

rigid in the sense that the energy barriers separating the positive- and negative- $\gamma$  minima are in general higher for Ru than that of Mo isotopes. For Mo isotopes with  $N \leq 58$  the ground states are calculated to be spherical.

One has to be careful in interpreting the results of the Mo isotopes. The softness of the total energy of a nucleus with respect to certain deformation degree of freedom indicates that the single-Slater description provided by the HF or HFB method may no longer be valid. One of the appropriate cures of such a problem is to solve the Hill-Wheeler equation [80] using multiple Slater determinants representing HF/HFB solutions that are constrained at a range of deformation values (multi-reference DFT or Generator coordinate method) [30]. Such a description is outside the scope of the current work.

## 3. Dynamical results for deformed nuclei

A good description for the IV  $E1$  photoabsorption cross section using the current TDDFT method gives confidence in the predictions for neutron-rich Zr, Mo, and Ru isotopes with  $N = 60 - 68$ . The predictions are displayed in Figs. 12 and 13. These dynamic calculation are performed without pairing interaction as the structures of the GDR peaks are essentially independent of pairing. To achieve fast and better convergence, we have imported single-particle wave functions from the HF calculations using the HFODD code. These HF calculations using the HO basis and the finite-difference method are both without deformation constraint. For triaxially deformed minima, the HF calculations give small  $\gamma$  differences compared to that of the HFB+LN results using HFODD. Specifically, for the softest nucleus, the triaxially deformed  $^{110}\text{Mo}$ , the HFB+LN calculation using HFODD gives quadrupole moments ( $Q_{20}^{\text{HFB+LN}}, Q_{22}^{\text{HFB+LN}}$ )  $\approx (8.5, 3.5)$  b (see Fig. 10). Without pairing, the HFODD calculation gives ( $Q_{20}^{\text{HF}}, Q_{22}^{\text{HF}}$ )  $\approx (9.4, 4.0)$  b. Before performing dynamic calculation, the static HF calculation in Cartesian coordinate space gives ( $Q_{20}^{\text{static}}, Q_{22}^{\text{static}}$ )  $\approx (9.5, 4.0)$  b.

The effect of the deformation on the GDR peak has been well known [38]. For tin isotopes with extreme neutron excess, the QRPA calculations based on the relativistic mean field [81] have been studied. Recent large-scale RPA calculations [22, 25] have been performed for light and medium-heavy nuclei. For both of these calculations, the effect of the deformation on the GDR peak, as well as the PDR contributions are carefully analyzed in connection with the neutron excess. The current dynamical calculations allow for analysis of IVD resonances in the context of nuclear shape evolution within the isotopic chains and shape coexistence in the same nucleus.

For a spherical nucleus the GDR peaks corresponding to the three vibrational modes are identical due to the same density profiles along the three axes. When the nucleus acquires a prolate deformation, the originally identical GDR peaks split into two groups: (1) a mode

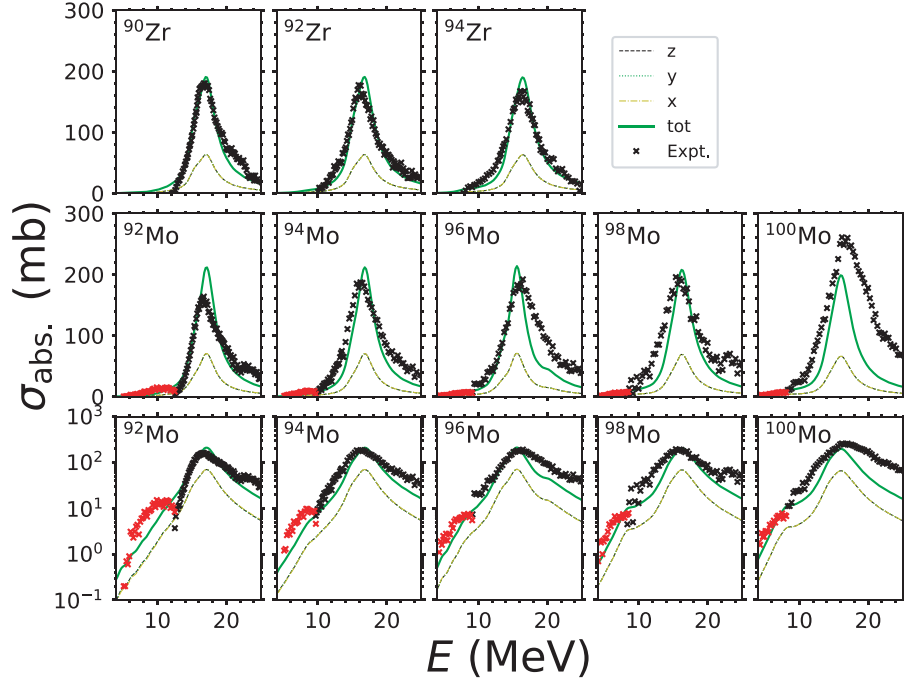


FIG. 8: Calculated photoabsorption cross sections using UNEDF1 EDF, with smoothing parameter  $\Gamma = 2.0$  MeV. The experimental data for GDR (black crosses) are from Refs. [63, 64]. The data for the lower-energy parts (red crosses) are from Refs. [65–67]. The numbers are extracted from Refs. [69, 70].

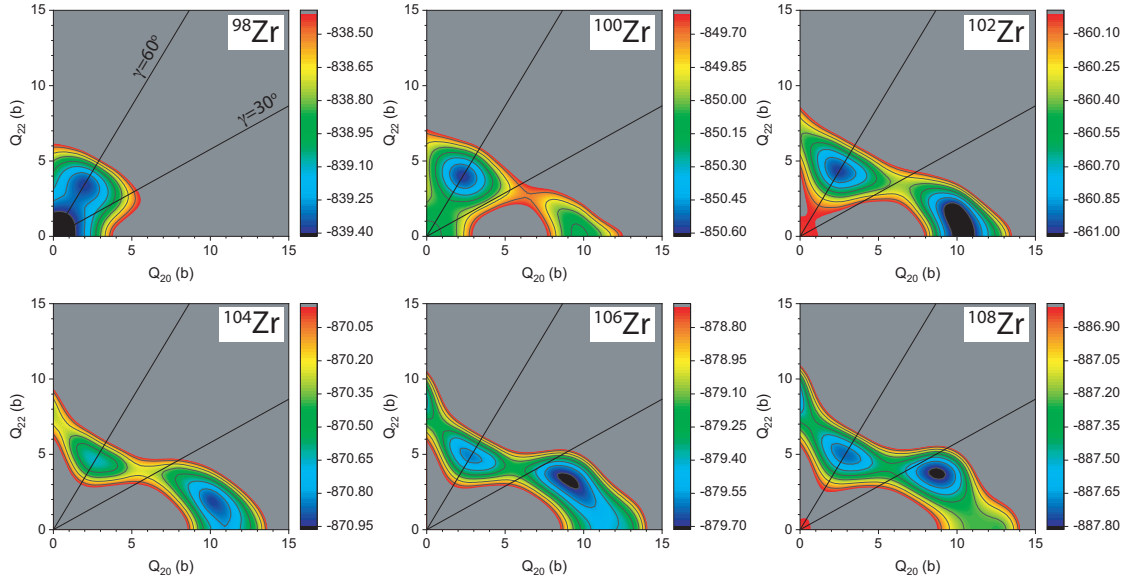


FIG. 9: Calculated potential-energy surfaces for  $^{98-108}\text{Zr}$ , using the UNEDF1 EDF. The energies are in MeV.

corresponding to a vibration along the symmetry axis ( $K = 0$  mode); and (2) two modes corresponding to the vibrations along the axes perpendicular to the symmetry axis ( $K = \pm 1$  modes). For a prolate shape, intuitively, because of the larger material extension, the potential is wider along the symmetry axis. Hence, the energy cost is lower for the  $K = 0$  mode, compared to the  $K = \pm 1$  modes. While the peak for the  $K = 0$  mode shifts to

lower energy, the contribution of this mode to the total strength becomes higher than those of the  $K = \pm 1$  modes. Similar effects can be found from light to heavy spherical nuclei, where the total GDR peak shifts to a lower energy and becomes taller and/or broader.

Due to the above-mentioned reasons, for an oblate deformation, the peaks corresponding to the  $K = \pm 1$  modes become higher and shift to lower excitation ener-

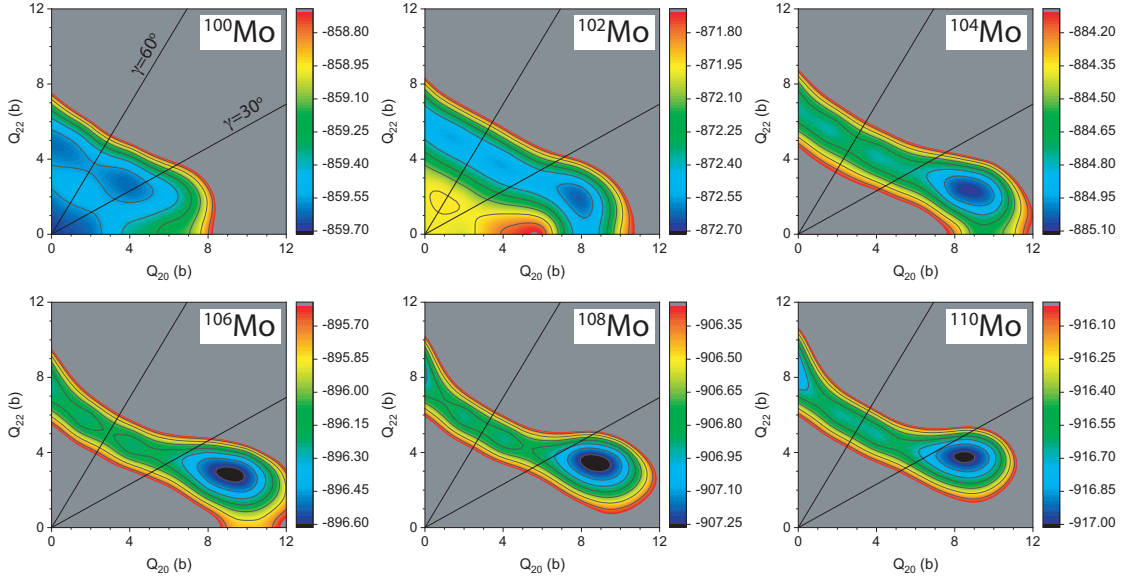


FIG. 10: The same as Fig. 9, except for  $^{100-110}\text{Mo}$ .

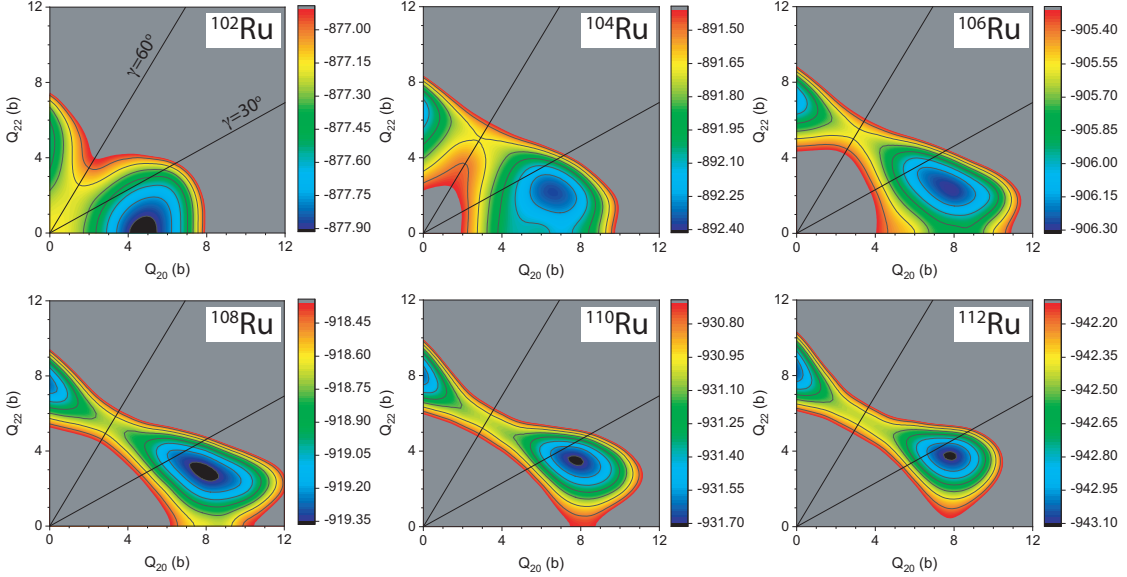


FIG. 11: The same as Fig. 9, except for  $^{102-112}\text{Ru}$ .

gies compared to that corresponding to the  $K = 0$  mode. We find all these features of the GDR peaks for prolate and oblate deformed  $^{100,102}\text{Zr}$  as shown in Fig. 12.

For  $^{104,106,108}\text{Zr}$ ,  $^{100-110}\text{Mo}$ , and  $^{102-112}\text{Ru}$  nuclei, the IVD vibrations are based on the triaxial minima, see Figs. 12 and 13. Due to the large smoothing parameter,  $\Gamma = 2.0 \text{ MeV}$ , the peaks at higher excitation energies appear to be one taller and broader peak compared to the lower-energy one. For  $^{110}\text{Mo}$  and  $^{108}\text{Zr}$ , the three peaks corresponding to  $x$ -,  $y$ -, and  $z$ -axis, merge into one broader peak.

Figure 14 plots the fraction of the IVD strength below  $E_c = 10 \text{ MeV}$  for zirconium isotopes based on dif-

ferent deformations. With the same deformation, the  $f_{\text{PDR}}$  values increase with neutron excess. From spherical to deformed nuclei, we see a small decrease of the  $f_{\text{PDR}}$  value at  $N = 60$ , which agrees with previous studies [22, 25]. This is a net result of (1) the decrease of energy of the  $K = 0$  mode, and the increase of the energy of the  $K = \pm 1$  modes, as well as (2) an enhanced contribution in the total strength from the  $K = 0$  mode, as pointed out in Ref. [81]. For the oblate deformation, there is a plateau structure below  $E = 10 \text{ MeV}$ , which is the main contribution to the  $f_{\text{PDR}}$  value. For spherical Mo isotopes, one can observe similar plateau structure at lower-energy part as shown in Fig. 8.

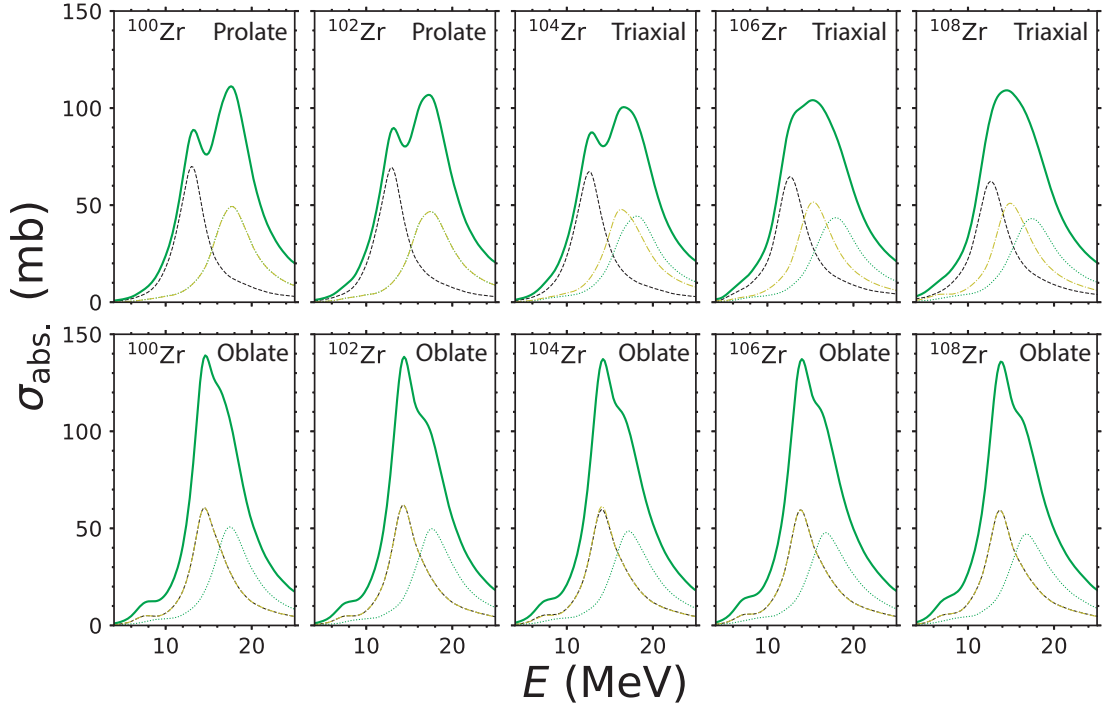


FIG. 12: Similar to Fig. 8, except for  $^{100-108}\text{Zr}$ . The plots in upper row correspond to the results based on the prolate minima for  $^{100,102}\text{Zr}$ , and the triaxial minima for  $^{104-108}\text{Zr}$ ; the plots in the lower row correspond to those based on the oblate minima, see Fig. (9).

#### IV. SUMMARY

Based on a previous computer code developed for the nuclear density-functional theory (DFT), we present a further development, enabling the time-dependent DFT (TDDFT) calculations. We benchmark the code by comparing its calculated response functions of dipole moment of  $^{16}\text{O}$  with that of an existing 3D TDDFT code, Sky3D. Although the response functions for  $^{16}\text{O}$  are sensitive to a few subtle factors (time-odd mean fields, treatment of boundary conditions, etc.), a remarkable agreement has been found between the two codes, as long as those factors are carefully considered.

To apply the TDDFT in its linearized limit and describe the isovector (IV) electric dipole ( $E1$ ) observables, we carry out finite-amplitude method for quasi-particle random-phase approximation (FAM-QRPA) for a few light spherical ( $^{16}\text{O}$ ,  $^{40}\text{Ca}$ ) and axially deformed ( $^{24,34}\text{Mg}$ ) nuclei, and compare the calculated IV  $E1$  properties with those resulted from TDDFT calculations. The comparisons are acceptable up to the first peak at  $E \approx 20$  MeV. Beyond that, the FAM-QRPA calculations give more fragmented peaks compared to that of the TDDFT calculations.

Using the UNEDF1 energy density functional (EDF), the current TDDFT calculations provide reasonable description for both the giant dipole resonance and the low-energy part of the IV  $E1$  photoabsorption cross section for spherical Zr and Mo nuclei, where experimental data

exist.

For heavier Zr isotopes, the calculated potential-energy surfaces show coexisting minima. The predicted  $E1$  photoabsorption cross sections reflect typical features depending on the local minima that they are based upon.

For heavier Mo and Ru isotopes, the ground states are triaxially deformed. The predicted cross sections show features that distinguish them from the spherical one. For Mo isotopes considered here, the predicted onset of the triaxial deformation which occurs in  $^{102}\text{Mo}$  ( $N = 60$ ), is only two neutrons larger than the isotope in which experimental data exist. The photo-nuclear experiments on these Mo isotopes are recommended.

#### Acknowledgments

Useful discussions with W. Nazarewicz and P. Stevenson are gratefully acknowledged. The current work is supported by National Natural Science Foundation of China (Grant No. 11705038), JSPS KAKENHI Grant No. 16K17680, the JSPS-NSFC Bilateral Program for the Joint Research Project on “Nuclear mass and life for unravelling mysteries of r-process”, and the Deutsche Forschungsgemeinschaft (DFG, German Research Foundation) - Projektnummer 279384907 - SFB 1245. YS thanks the HPC Studio at Physics Department of Harbin Institute of Technology for computing resources allocated through INSPUR-HPC@PHY.HIT. A part of the numer-

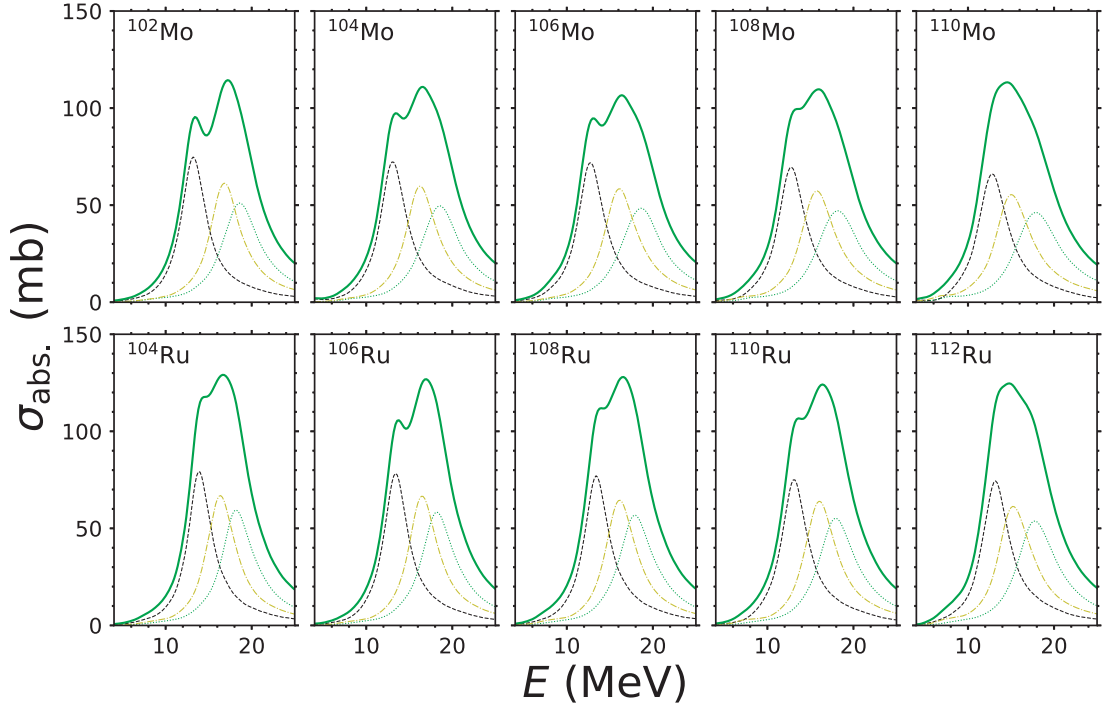


FIG. 13: The same as Fig. 12, except for  $^{102-110}\text{Mo}$  and  $^{104-112}\text{Ru}$ .

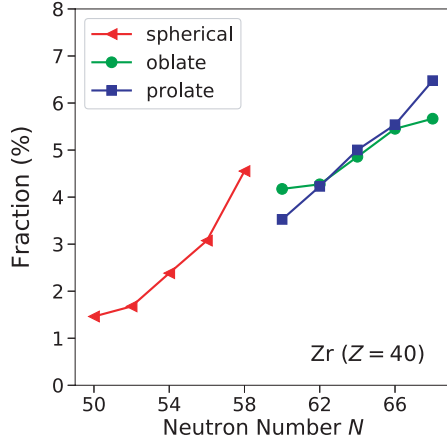


FIG. 14: The fraction of the strengths for IVD resonances below  $E_c = 10$  MeV [Eq. (32)] for zirconium isotopes with spherical, prolate and oblate deformations.

ical calculations were performed at the Oakforest-PACS Systems through the Multidisciplinary Cooperative Research Program of the Center for Computational Sciences, University of Tsukuba.

- 
- [1] Y. Engel, D. Brink, K. Goeke, S. Krieger, and D. Vautherin, Nucl. Phys. A **249**, 215 (1975).
  - [2] P. Bonche, S. E. Koonin, and J. W. Negele, Phys. Rev. C **13**, 1226 (1976).
  - [3] R. Y. Cusson, R. K. Smith, and J. A. Maruhn, Phys. Rev. Lett. **36**, 1166 (1976).
  - [4] J. W. Negele, Rev. Mod. Phys. **54**, 913 (1982).
  - [5] T. Nakatsukasa, K. Matsuyanagi, M. Matsuo, and K. Yabana, Rev. Mod. Phys. **88**, 045004 (2016).
  - [6] A. S. Umar, V. E. Oberacker, and C. Simenel, Phys. Rev. C **92**, 024621 (2015).
  - [7] C. Simenel, Eur. Phys. J. A **48**, 152 (2012).
  - [8] S. Burrello, M. Colonna, G. Colò, D. Lacroix, X. Roca-Maza, G. Scamps, and H. Zheng, Phys. Rev. C **99**, 054314 (2019).
  - [9] T. Nakatsukasa and K. Yabana, Phys. Rev. C **71**, 024301 (2005).
  - [10] J. A. Maruhn, P. G. Reinhard, P. D. Stevenson, J. R. Stone, and M. R. Strayer, Phys. Rev. C **71**, 064328 (2005).



- [11] A. S. Umar and V. E. Oberacker, Phys. Rev. C **73**, 054607 (2006).
- [12] I. Stetcu, A. Bulgac, P. Magierski, and K. J. Roche, Phys. Rev. C **84**, 051309 (2011).
- [13] A. Bulgac, P. Magierski, K. J. Roche, and I. Stetcu, Phys. Rev. Lett. **116**, 122504 (2016).
- [14] P. Magierski, K. Sekizawa, and G. Wlazłowski, Phys. Rev. Lett. **119**, 042501 (2017).
- [15] Y. Hashimoto, Eur. Phys. J. A **48**, 55 (2012).
- [16] Y. Hashimoto, Phys. Rev. C **88**, 034307 (2013).
- [17] K. Washiyama and T. Nakatsukasa, Phys. Rev. C **96**, 041304 (2017).
- [18] Y. Shi, Phys. Rev. C **98**, 014329 (2018).
- [19] J. Dobaczewski and J. Dudek, Comput. Phys. Commun. **102**, 166 (1997).
- [20] J. Dobaczewski, W. Satuła, B. Carlsson, J. Engel, P. Olbratowski, P. Powalowski, M. Sadziak, J. Sarich, N. Schunck, A. Staszczak, M. Stoitsov, M. Zalewski, and H. Zduniczuk, Comput. Phys. Commun. **180**, 2361 (2009).
- [21] N. Schunck, J. Dobaczewski, W. Satuła, P. Baczyk, J. Dudek, Y. Gao, M. Konieczka, K. Sato, Y. Shi, X. Wang, and T. Werner, Comput. Phys. Commun. **216**, 145 (2017).
- [22] T. Inakura, T. Nakatsukasa, and K. Yabana, Phys. Rev. C **84**, 021302 (2011).
- [23] G. Scamps and D. Lacroix, Phys. Rev. C **88**, 044310 (2013).
- [24] G. Scamps and D. Lacroix, Phys. Rev. C **89**, 034314 (2014).
- [25] S. Ebata, T. Nakatsukasa, and T. Inakura, Phys. Rev. C **90**, 024303 (2014).
- [26] J. Kvasil, P. Vesely, V. O. Nesterenko, W. Kleinig, P.-G. Reinhard, and S. Frauendorf, Int. J. Mod. Phys. E **18**, 975 (2009).
- [27] B. Schuetrumpf, P. G. Reinhard, P. D. Stevenson, A. S. Umar, and J. A. Maruhn, Comput. Phys. Commun. **229**, 211 (2018).
- [28] J. Maruhn, P.-G. Reinhard, P. Stevenson, and A. Umar, Comput. Phys. Commun. **185**, 2195 (2014).
- [29] J. Bardeen, L. N. Cooper, and J. R. Schrieffer, Phys. Rev. **108**, 1175 (1957).
- [30] P. Ring and P. Schuck, *The Nuclear Many-Body Problem* (Springer-Verlag, Berlin, 1980).
- [31] M. Bender, K. Rutz, P.-G. Reinhard, and J. Maruhn, Eur. Phys. J. A **8**, 59 (2000).
- [32] J. Dobaczewski, H. Flocard, and J. Treiner, Nucl. Phys. A **422**, 103 (1984).
- [33] S. Fracasso, E. B. Suckling, and P. D. Stevenson, Phys. Rev. C **86**, 044303 (2012).
- [34] L. Guo, C. Simenel, L. Shi, and C. Yu, Phys. Lett. B **782**, 401 (2018).
- [35] J. Dobaczewski and J. Dudek, Phys. Rev. C **52**, 1827 (1995).
- [36] B. Schuetrumpf and W. Nazarewicz, Phys. Rev. C **92**, 045806 (2015).
- [37] C. Q. He, J. C. Pei, Y. Qiang, and N. Fei, Phys. Rev. C **99**, 054318 (2019).
- [38] M. N. Harakeh and A. van der Woude, *Giant Resonances: Fundamental High-Frequency Modes of Nuclear Excitation* (Oxford University Press, London, 2001).
- [39] P. Stevenson, private communication, 2020.
- [40] K. Yoshida and T. Nakatsukasa, Phys. Rev. C **83**, 021304 (2011).
- [41] T. Oishi, M. Kortelainen, and N. Hinohara, Phys. Rev. C **93**, 034329 (2016).
- [42] N. Hinohara, M. Kortelainen, W. Nazarewicz, and E. Olsen, Phys. Rev. C **91**, 044323 (2015).
- [43] N. Hinohara, Phys. Rev. C **100**, 024310 (2019).
- [44] A. Bohr and B. R. Mottelson, *Nuclear Structure, vol. II* (W. A. Benjamin, Reading, 1975).
- [45] J. Bartel, P. Quentin, M. Brack, C. Guet, and H.-B. Håkansson, Nucl. Phys. A **386**, 79 (1982).
- [46] M. Kortelainen, J. McDonnell, W. Nazarewicz, P.-G. Reinhard, J. Sarich, N. Schunck, M. V. Stoitsov, and S. M. Wild, Phys. Rev. C **85**, 024304 (2012).
- [47] J. Piekarewicz, Phys. Rev. C **73**, 044325 (2006).
- [48] T. Inakura, T. Nakatsukasa, and K. Yabana, Phys. Rev. C **80**, 044301 (2009).
- [49] Q. Wu, B. S. Hu, F. R. Xu, Y. Z. Ma, S. J. Dai, Z. H. Sun, and G. R. Jansen, Phys. Rev. C **97**, 054306 (2018).
- [50] K. Liu and N. V. Giai, Phys. Lett. B **65**, 23 (1976).
- [51] T. Nakatsukasa, T. Inakura, and K. Yabana, Phys. Rev. C **76**, 024318 (2007).
- [52] P. Avogadro and T. Nakatsukasa, Phys. Rev. C **84**, 014314 (2011).
- [53] M. Kortelainen, N. Hinohara, and W. Nazarewicz, Phys. Rev. C **92**, 051302(R) (2015).
- [54] M. Stoitsov, J. Dobaczewski, W. Nazarewicz, and P. Ring, Comput. Phys. Commun. **167**, 43 (2005).
- [55] M. Stoitsov, N. Schunck, M. Kortelainen, N. Michel, H. Nam, E. Olsen, J. Sarich, and S. Wild, Comput. Phys. Commun. **184**, 1592 (2013).
- [56] R. N. Perez, N. Schunck, R.-D. Lasserri, C. Zhang, and J. Sarich, Comput. Phys. Commun. **220**, 363 (2017).
- [57] S. Péru and H. Goutte, Phys. Rev. C **77**, 044313 (2008).
- [58] C. Losa, A. Pastore, T. Døssing, E. Vigezzi, and R. A. Broglia, Phys. Rev. C **81**, 064307 (2010).
- [59] M. Stoitsov, M. Kortelainen, T. Nakatsukasa, C. Losa, and W. Nazarewicz, Phys. Rev. C **84**, 041305 (2011).
- [60] S. Ebata, T. Nakatsukasa, T. Inakura, K. Yoshida, Y. Hashimoto, and K. Yabana, Phys. Rev. C **82**, 034306 (2010).
- [61] L.-G. Cao and Z.-Y. Ma, Phys. Rev. C **71**, 034305 (2005).
- [62] K. Wang, M. Kortelainen, and J. C. Pei, Phys. Rev. C **96**, 031301 (2017).
- [63] B. L. Berman, J. T. Caldwell, R. R. Harvey, M. A. Kelly, R. L. Bramblett, and S. C. Fultz, Phys. Rev. **162**, 1098 (1967).
- [64] H. Beil, R. Bergère, P. Carlos, A. Leprêtre, A. D. Miniac, and A. Veyssière, Nucl. Phys. A **227**, 427 (1974).
- [65] G. Rusev, E. Grosse, M. Erhard, A. Junghans, K. Kosev, K. D. Schilling, R. Schwengner, and A. Wagner, Eur. Phys. J. A **27**, 171 (2006).
- [66] G. Rusev, R. Schwengner, F. Döna, M. Erhard, E. Grosse, A. R. Junghans, K. Kosev, K. D. Schilling, A. Wagner, F. Bečvář, and M. Krčička, Phys. Rev. C **77**, 064321 (2008).
- [67] M. Erhard, A. R. Junghans, C. Nair, R. Schwengner, R. Beyer, J. Klug, K. Kosev, A. Wagner, and E. Grosse, Phys. Rev. C **81**, 034319 (2010).
- [68] V. O. Nesterenko, W. Kleinig, J. Kvasil, P. Vesely, P.-G. Reinhard, and D. S. Dolci, Phys. Rev. C **74**, 064306 (2006).
- [69] Russia Lomonosov Moscow State University Skobel'syn Institute of Nuclear Physics Centre for Photonuclear Experiments Data database, Nuclear Reaction Database (EXFOR), <http://cdfc.sinp.msu.ru/exfor/index.php>.



- [70] USA National Nuclear Data Center database CSISRS and EXFOR Nuclear reaction experimental data, <http://www.nndc.bnl.gov/exfor/exfor00.htm>.
- [71] T. Togashi, Y. Tsunoda, T. Otsuka, and N. Shimizu, *Phys. Rev. Lett.* **117**, 172502 (2016).
- [72] J. Zhao, B.-N. Lu, E.-G. Zhao, and S.-G. Zhou, *Phys. Rev. C* **95**, 014320 (2017).
- [73] T. Nakamura, H. Sakurai, and H. Watanabe, *Prog. Part. Nucl. Phys.* **97**, 53 (2017).
- [74] H. Watanabe, K. Yamaguchi, A. Odahara, T. Sumikama, S. Nishimura, K. Yoshinaga, Z. Li, Y. Miyashita, K. Sato, L. Próchniak, H. Baba, J. Berryman, N. Blasi, A. Bracco, F. Camera, J. Chiba, P. Doornenbal, S. Go, T. Hashimoto, S. Hayakawa, C. Hinke, N. Hinohara, E. Ideguchi, T. Isobe, Y. Ito, D. Jenkins, Y. Kawada, N. Kobayashi, Y. Kondo, R. Krücken, S. Kubono, G. Lorusso, T. Nakano, T. Nakatsukasa, M. Kurata-Nishimura, H. Ong, S. Ota, Z. Podolyák, H. Sakurai, H. Scheit, K. Steiger, D. Steppenbeck, K. Sugimoto, K. Tajiri, S. Takano, A. Takashima, T. Teranishi, Y. Wakabayashi, P. Walker, O. Wieland, and H. Yamaguchi, *Phys. Lett. B* **704**, 270 (2011).
- [75] N. Paul, A. Corsi, A. Obertelli, P. Doornenbal, G. Authalet, H. Baba, B. Bally, M. Bender, D. Calvet, F. Château, S. Chen, J.-P. Delaroche, A. Delbart, J.-M. Gheller, A. Giganon, A. Gillibert, M. Girod, P.-H. Heenen, V. Lapoux, J. Libert, T. Motobayashi, M. Niikura, T. Otsuka, T. R. Rodríguez, J.-Y. Roussé, H. Sakurai, C. Santamaria, N. Shimizu, D. Steppenbeck, R. Taniuchi, T. Togashi, Y. Tsunoda, T. Uesaka, T. Ando, T. Arici, A. Blazhev, F. Browne, A. M. Bruce, R. Carroll, L. X. Chung, M. L. Cortés, M. Dewald, B. Ding, F. Flavigny, S. Franchoo, M. Górska, A. Gottardo, A. Jungclauss, J. Lee, M. Lettmann, B. D. Linh, J. Liu, Z. Liu, C. Lizarazo, S. Momiyama, K. Moschner, S. Nagamine, N. Nakatsuka, C. Nita, C. R. Nobs, L. Olivier, Z. Patel, Z. Podolyák, M. Rudigier, T. Saito, C. Shand, P.-A. Söderström, I. Stefan, R. Orlandi, V. Vaquero, V. Werner, K. Wimmer, and Z. Xu, *Phys. Rev. Lett.* **118**, 032501 (2017).
- [76] D. Doherty, J. Allmond, R. Janssens, W. Korten, S. Zhu, M. Zielińska, D. Radford, A. Ayangeakaa, B. Bucher, J. Batchelder, C. Beausang, C. Campbell, M. Carpenter, D. Cline, H. Crawford, H. David, J. Delaroche, C. Dickerson, P. Fallon, A. Galindo-Uribarri, F. Kondev, J. Harker, A. Hayes, M. Hendricks, P. Humby, M. Girod, C. Gross, M. Klintefjord, K. Kolos, G. Lane, T. Lauritsen, J. Libert, A. Macchiavelli, P. Napiorkowski, E. Padilla-Rodal, R. Pardo, W. Reviol, D. Sarantites, G. Savard, D. Seweryniak, J. Srebrny, R. Varner, R. Vondrasek, A. Wiens, E. Wilson, J. Wood, and C. Wu, *Phys. Lett. B* **766**, 334 (2017).
- [77] C. L. Zhang, G. H. Bhat, W. Nazarewicz, J. A. Sheikh, and Y. Shi, *Phys. Rev. C* **92**, 034307 (2015).
- [78] G. Bhat, J. Sheikh, Y. Sun, and R. Palit, *Nucl. Phys. A* **947**, 127 (2016).
- [79] J. Xiang, J. M. Yao, Y. Fu, Z. H. Wang, Z. P. Li, and W. H. Long, *Phys. Rev. C* **93**, 054324 (2016).
- [80] D. L. Hill and J. A. Wheeler, *Phys. Rev.* **89**, 1102 (1953).
- [81] D. P. n. Arteaga, E. Khan, and P. Ring, *Phys. Rev. C* **79**, 034311 (2009).